Wind Tunnel Experiment of Microjet-based Flow Control on a Multi-Element High-Lift Airfoil

C.P. van Dam[1] and Sai Bharath Mothukuri[2]
University of California–Davis, Davis, CA 95616

Seyedeh Sheida Hosseini[3]
NASA Ames Research Center, Moffett Field, CA 94035

Edward B. White,[4] Lisa M. Brown[5], Douglas M. Kutz[5], Ezequiel Justiniano[6]
Texas A&M University, College Station, TX 77843-3141

A wind tunnel model was designed, manufactured, and tested to evaluate the potential of active aerodynamic flow control for multi-element airfoils. The active flow control system involves so-called microjets – small, low momentum, normal to the surface jets located near the trailing edge of the flap – for controlling the lift and improving the aerodynamic performance characteristics of airplane high-lift systems. The configuration selected for this test is the NLR7301 two-element airfoil and it was tested in the Oran W. Nicks Low-Speed Wind Tunnel at Texas A&M University at a chord Reynolds number of 2.0 million and Mach number of 0.10. This paper presents wind tunnel results for the NLR7301 in the Flap 20 and Flap 30 configurations. The wind tunnel results include surface pressure distributions, lift and pitching moment, and flow visualizations. The results of this experiment validate the effectiveness of the microjet with regards to control of lift in the linear regime for multi-element airfoils.

I. Nomenclature

A^*	Throat area of the critical flow venturi
b	Span = 83 in.
C_p	Pressure coefficient = $\frac{p-p_\infty}{q_\infty}$
C_q	Mass flow coefficient = $\frac{\dot{m}}{\rho_\infty U_\infty S}$
C_μ	Momentum coefficient = $\frac{\dot{m}\, U_j}{q_\infty S}$
c	Model reference chord = 36 in.
c_{flap}	Flap chord = 12 in.
c_l	Lift coefficient = $\frac{L'}{q_\infty c}$
c_m	Pitching moment coefficient about 0.25c = $\frac{M'}{q_\infty c^2}$
L'	Sectional lift from surface pressures
M'	Sectional pitching moment about 0.25c from surface pressures
M	Mach number
$\dot{m}$	Mass flow rate of active flow control system
n	Boundary layer transition criterion, critical amplification ratio
p	Pressure
q	Dynamic pressure = $\frac{\rho U^2}{2}$

[1] Professor Emeritus, Department of Mechanical and Aerospace Engineering. Associate Fellow AIAA.
[2] Graduate Research Assistant, Department of Mechanical and Aerospace Engineering.
[3] Research Aerospace Engineer, Computational Aerosciences Branch. Member AIAA.
[4] Professor, Department of Aerospace Engineering. Associate Fellow AIAA.
[5] Test Engineer, Department of Aerospace Engineering. Member AIAA.
[6] Graduate Research Assistant, Department of Aerospace Engineering.

Re Reynolds number = $\frac{\rho_\infty U_\infty c}{\mu_\infty}$
S Reference area = 2,988 in^2
T Air temperature
U Airspeed
α Angle of attack
ρ Air density
σ Standard deviation
μ Absolute viscosity

Subscript:
∞ Freestream condition
j Microjet
t Total

II. Introduction

This paper focuses on the potential of microjets for controlling the lift and improving the aerodynamic performance characteristics of airplane high-lift systems. Microjets are small, nominally-orthogonal jets located near the trailing edge of the flaps used during takeoff and landing. Computational Fluid Dynamics (CFD) simulations indicate that these microjets will increase the lift coefficient and may also reduce the drag coefficient, increasing the lift-to-drag ratio.[1,2] Lift enhancement has been predicted and experimentally observed for single element airfoils by Malavard et al.[3,4], Boeije et al.[5] and Blaylock et al.[6] but the concept has not been tested on the flap of a multi-element airfoil. CFD simulations (Fig. 1) indicate that a low momentum microjet on the lower surface close to the trailing edge of a flap could increase lift and reduce drag, with a relatively low operating pressure requirement.[1,2] These performance enhancements would enable improvements to the overall airplane design (e.g., control of tail clearance angle) and performance (e.g., shorter field lengths, or higher payloads).[7,8]

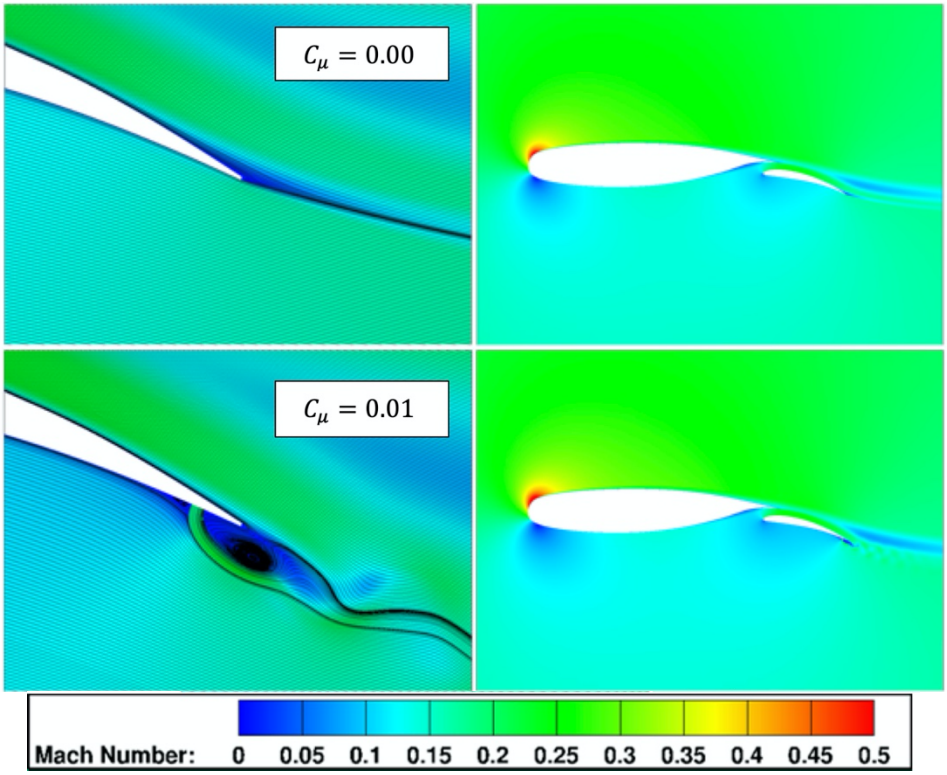

Fig. 1 CFD flow visualizations for NLR7301 multi-element airfoil with microjet located at 95% of the flap chord: (top) no jet; (bottom) microjet on lower surface increases lift.[1,2]

Accurate characterization of microjet performance based on experimental results is an important step in evaluating the potential for application of this device to future airplanes. In addition to validating CFD predictions of aerodynamic performance, wind tunnel tests allow for realistic evaluations of the power, air mass flow rate and operating pressure required for a microjet system. If potential gains in high-lift performance are realized, they will advance progress towards more efficient and flexible future air vehicles as envisioned in NASA ARMD's Strategic Thrust 3: Ultra-Efficient Commercial Vehicles.

In the following chapter, the overall technical approach, model design and manufacturing are discussed. Next, results acquired in the wind tunnel at Texas A&M are presented. Finally, conclusions are presented, and next steps are outlined.

III. Experimental Setup

The technical approach followed for this project was to design, build and test an airfoil model with flap microjets in a wind tunnel. The design phase of this project began in FY19 with the design shown in Fig. 2. The model has a constant cross-sectional profile based on the NLR7301 airfoil with flap.[9] Compressed air is delivered to the flap trailing edge via internal channels in the flap element that connect to an external air supply through openings at either end of the flap. Figure 3 depicts sample CFD-based internal flow patterns for the flap.

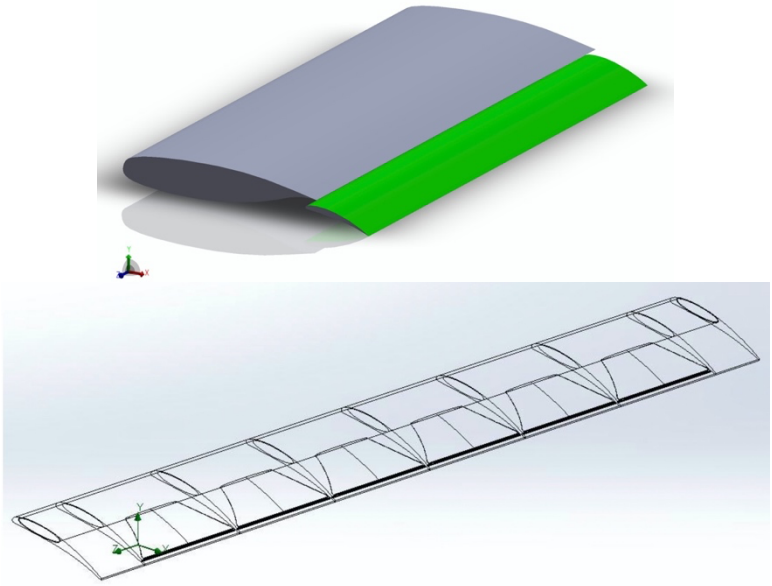

Fig. 2 Wind tunnel model design images: (top) Main element (gray) and flap (green) of NLR7301 airfoil with 20° flap deflection; (bottom) Transparent view of the flap showing internal flow channels.

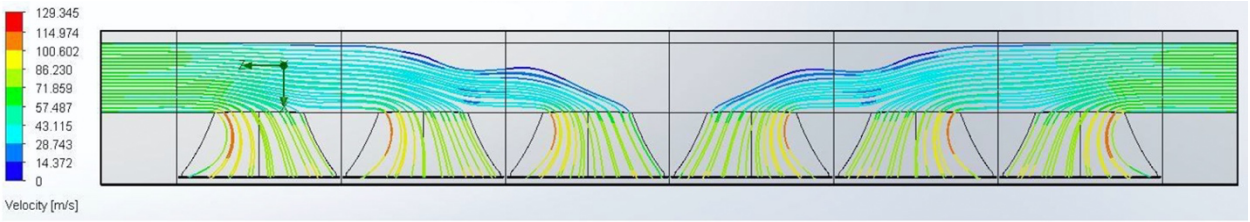

Fig. 3 CFD-based internal flow velocity pattern for the flap. Microjet slot width = 0.25% c = 0.09 in. Total slot span = 6 × 11.75 = 70.5 in. = 85% of model span. Total slot area = 6.35 in^2.

A. Section Shape

Benchmark experimental results are available for the NLR7301 flapped airfoil (Fig. 4). In the benchmark wind tunnel tests conducted by the NLR in the 1970s, the flap has a deflection angle of 20°. Because the geometry and detailed wind tunnel results are available for this configuration, it was used by Hosseini for her study on active flow control.[1,2] Also, it was selected because its high-lift performance and flap thickness are comparable to airfoils used on

state-of- the-art commercial transport airplanes**.** The wind-tunnel results for this airfoil contain wall corrections and include detailed aerodynamic results at an angle of attack of 6 degrees, a Reynolds number based on the reference chord c of 2.51 million and freestream Mach number of 0.185. The normalized airfoil geometry is shown in Fig. 4 where the cruise chord (= reference chord), c, is unity and c_{flap} = 32% of c. The gap and overlap for this geometry are reported as 2.6% and 5.3% of c, respectively.

NLR designed the flap in the above configuration to have mostly attached flow. However, to investigate the impact of flow separation on microjet effectiveness, the flap was deflected an additional 10 degrees while retaining the gap and overlap settings from the 20 deg configuration. It is important to note that there are no published experimental data for the NLR7301 with 30 deg flap deflection but the CFD results of Hosseini et al.[2] indicate the flow over the aft approximately 11% of the suction side flap chord to be separated.

B. Wind Tunnel

The NLR7301 wind tunnel model was tested in the Oran W. Nicks Low-Speed WindTunnel (LSWT) at Texas A&M University.[10] We considered relevant limits and parameters for the LSWT while making initial design choices for the model. Nominal values for the model reference chord and span were 32 in. and 83 in., respectively. However, the reference chord was adjusted to 36 in. during the design process to provide more volume for the flow control conduits in the flap and to obtain a slightly higher test Reynolds number. The airfoil is installed vertically in the test section with lift and pitching moment determined from surface pressure measurements and profile drag from wake rake measurements.

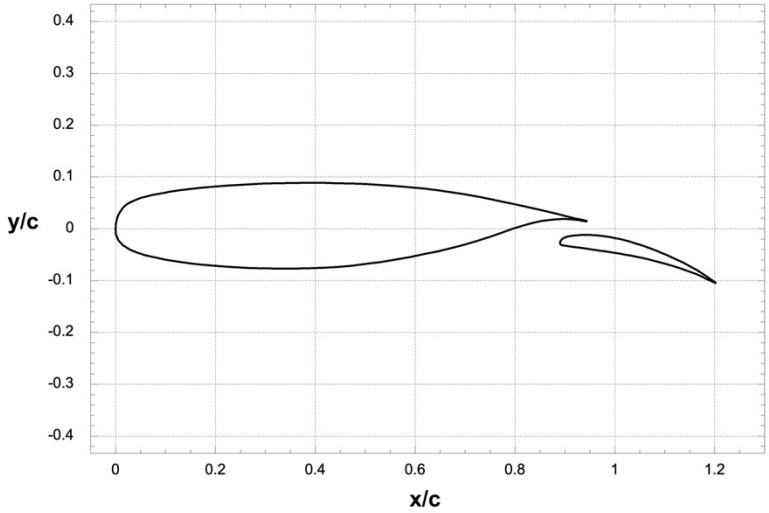

Fig. 4 NLR7301 in Flap 20 configuration.[9]

C. Wind Tunnel Model

The model has a constant cross-sectional profile based on the NLR7301 airfoil with flap as shown in Fig. 2 with the flap modified for the current test as detailed below. The chord of its main element is 34 in., and the chord of its flap is 12 in., while the span is 83 in. The spanwise length was set based on wind tunnel test section dimensions, while the chord length represents a compromise between limiting the maximum aerodynamic forces while making the flap large enough to incorporate internal channels for supplying air to the microjets. Note, the reference chord is 36 in. and is based on the chord of the airfoil in cruise with the flap retracted.

The original flap used by Van den Berg[9] is thin (maximum t/c ≈ 0.09) and highly cambered, which complicates the design of the microjet supply plumbing. Cooperman et al.[11] evaluated the performance of the NLR7301 airfoil with modified (slightly thicker) flap profiles. They applied XFOIL[12] to modify the original flap profile by increasing the trailing edge thickness from $0.0036c_{flap}$ to $0.0072c_{flap}$ (denoted "2× TE") and $0.0144c_{flap}$ ("4× TE"). In each case, a wedge was added to both the upper and lower surfaces of the flap, starting at the leading edge with zero thickness and widening smoothly to the prescribed thickness at the trailing edge. The position of the modified flaps was then selected such that the modified upper surface aligned with the upper surface of the original flap thereby retaining the rigging of the original flap. Figure 5a depicts the original flap and the modified flap at the 20-degree flap setting.

Each configuration was simulated in MSES.[13] For a given angle of attack, the lift coefficient increases slightly

with trailing edge thickness, with $\Delta c_l \approx 0.02$ for the 2× TE flap and $\Delta c_l \approx 0.05$ for the 4× TE flap in the linear portion of the lift curve. The drag coefficient does not show a significant change with flap thickness in this region. Examination of the surface pressure distribution for the case of $\alpha = 6°$ indicates increased suction on the upper surface of the 4× TE flap, with a slightly steeper pressure gradient on the lower surface.

Figure 5b depicts the airfoil with the modified (4× TE) flap in the Flap 20 and Flap 30 configuration. The wind-tunnel model provides these two flap configurations by means of two different sets of four CNC-machined flap brackets. The brackets are visible in smoke flow images shown in Section IV.D.

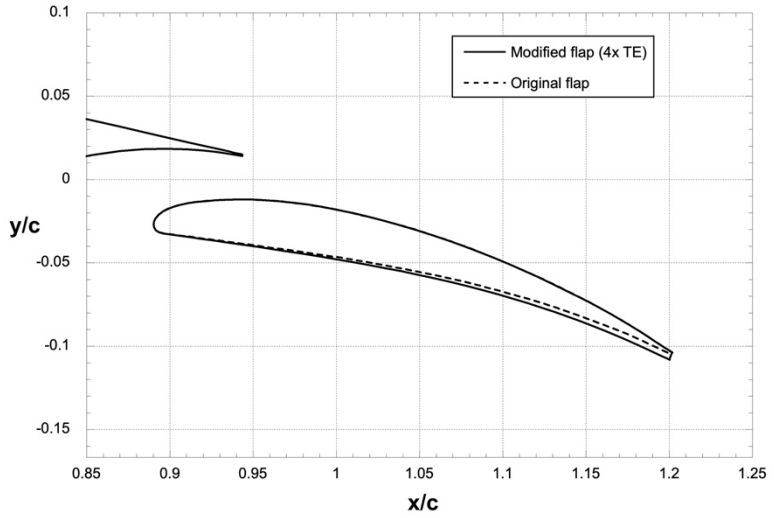

(a) Comparison of original flap NLR7301 airfoil and 4× TE flap (Flap 20).

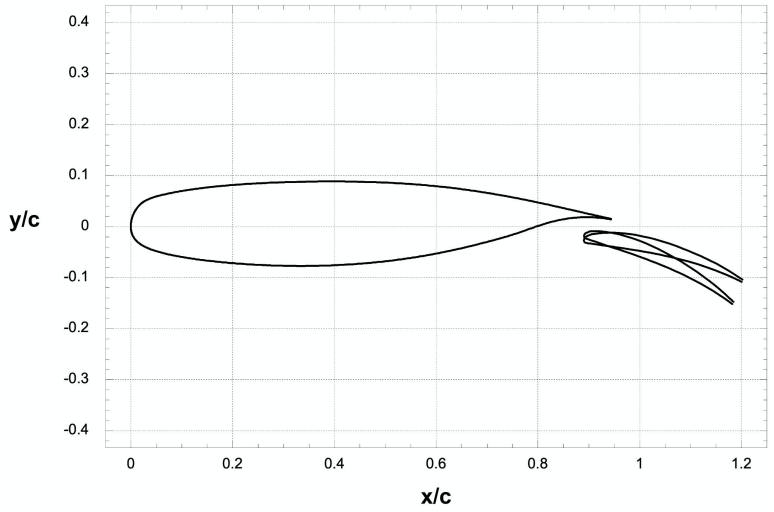

(b) Airfoil with modified flap in Flap 20 and Flap 30 configuration.

Fig. 5 Flap geometry modification and configurations.

Air for the flow control system is provided through elliptical openings at both ends of the 83 in. flap (Fig. 6). The resulting spanwise plenum is placed towards the leading edge of the flap and has a cross sectional area of 3.66 in^2. This flap plenum acts as a channel for the air mass flow feeding the 6 spanwise modules as depicted in Figs. 2 and 3. The plenum is then connected to the microjet outlets using a chordwise duct, or conduit. The constant area conduit connects the plenum to the jet exit through a smooth progression of geometrically similar cross section areas. For this design, it was decided that the transition from the plenum to the microjet outlet would take place through a series of constant area super ellipses (based on the work by Burley et al.[14]) from an elliptical entry with specified ratio of minor axis to major axis at the conduit inlet to a rectangular microjet exit. Figures 7a and 7b depict the chordwise conduit in top view and side view. Each chordwise conduit has a constant cross-sectional area of 1.06 in^2. The microjet exit is

located at $0.95c_{flap}$ on the lower surface and has a width of 0.09 in. or 0.25% of c. The microjet slot is divided into six sections each spanning 11.75 in., for a total of 85% of the full model span. The remaining portion of the span is completed by two 5.5-in. endcaps. The total microjet exit area is 6 × 11.75 in. × 0.09 in. = 6.3 in^2.

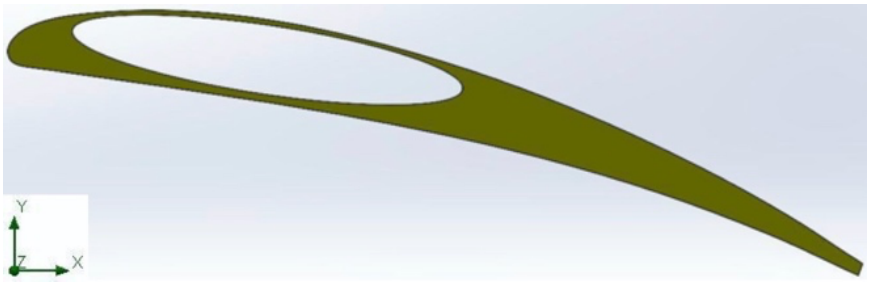

Fig. 6 Cross section of flap depicting the elliptical spanwise plenum.

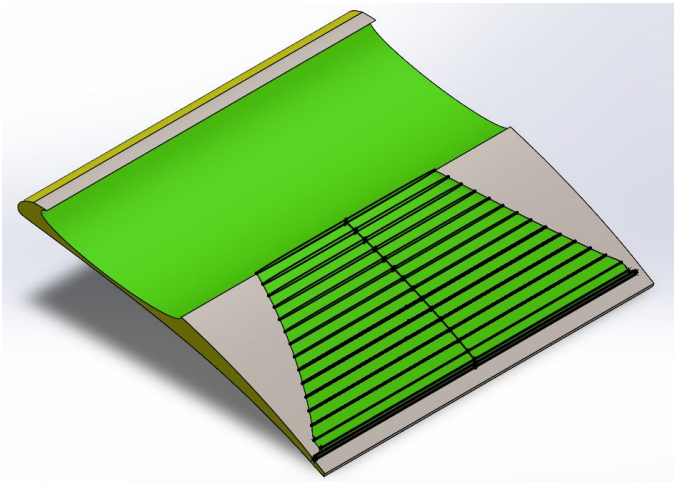

(a) Outline of constant cross-sectional area chordwise conduit (green with black stripes) connecting spanwise plenum (green) and microjet (black) near flap trailing edge.

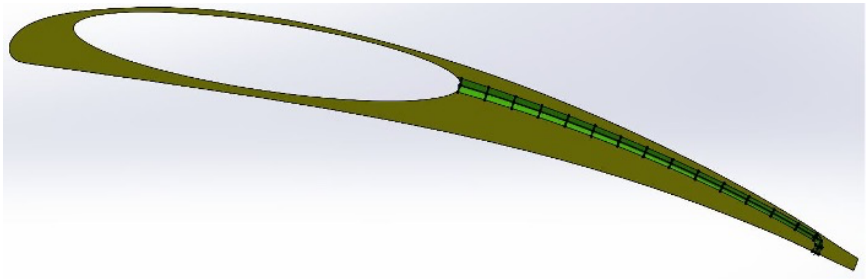

(b) Cross section of flap depicting the minor axis (black) and centerline of chordwise conduit connecting spanwise plenum and microjet.

Fig. 7 CAD images of chordwise conduit connecting spanwise plenum and microjet exit.

Figure 8 shows the pressure side flap panel as it was nearing completion at TAMU, where the Engineering Experiment Station operates a machine shop capable of building and modifying models for wind tunnel tests. The main wing is machined from AA 6061 whereas AA 7075 is used for the flap with steel the material used for the flap brackets and the keys connecting the main-element leading edge to suction and pressure side panels. Figure 8 depicts the flap when the pressure tubing still had to be installed with the flap pressure ports located in between the two middle chordwise conduits.

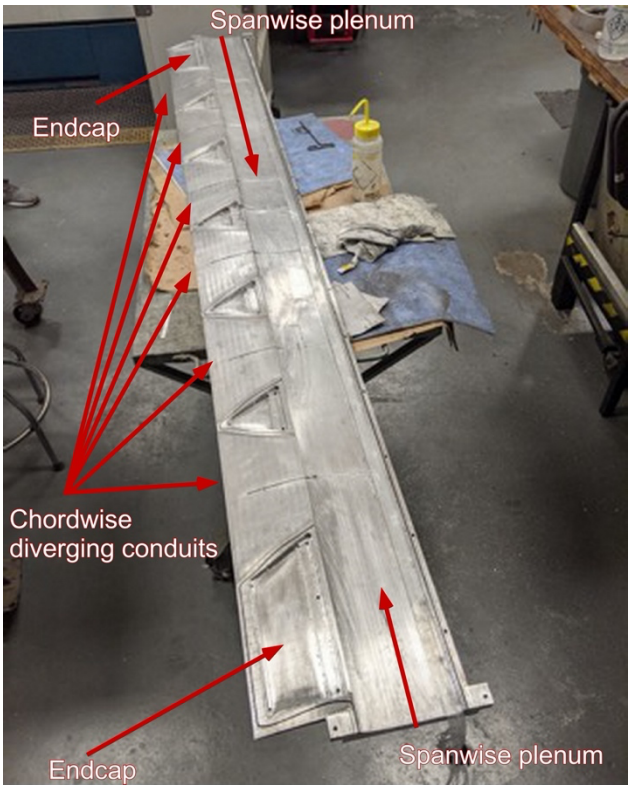

Fig. 8 Flap pressure side panel depicting the spanwise plenum, the two endcaps, and the six conduits connecting the plenum and the microjets.

Figures 9 and 10 show the main element of the NLR7301 model and the NLR7301 with the flap in the Flap 20 configuration, respectively, installed in the LSWT test section. Lift and pitching moment are computed using surface static pressure measurements made at multiple pressure taps on the main element and flap. The main element includes 53 static pressure ports located near the center of the model span that are used for load calculations in addition to 11 other ports used to confirm spanwise flow uniformity. The flap includes 28 static pressure ports used for load calculations. The flap ports are located in between the two central blowing modules. There may be spanwise variability in the slot blowing output that would not be detectable using the pressure ports. Future particle image velocimetry (PIV) measurements will investigate the velocity distribution in the trailing edge region of the flap and the possibility of spanwise variability of the jet outputs.

Fig. 9 Downstream view of NLR7301 main element installed in wind tunnel test section.

Fig. 10 Upstream view of NLR7301 two-element model installed in wind tunnel test section.

D. Tunnel Air Supply System

High pressure air from a high-pressure storage system (2,500 psi) supplies the air for the microjets. The volume and pressure of the storage system is sufficient to maintain a constant mass flow rate for the duration of an angle of attack sweep. The maximum total mass flow rate considered for the current wind tunnel test is $\dot{m}$ = 0.56 kg/s (1.23 lb/s). A schematic of the system is presented in Fig. 11.

A critical flow venturi in each line supplying the two ends of the flap controls the mass flow to the flap and its microjets. The supply lines from the split to the critical venturi has a diameter of 2.0 in. Using the choked flow equation:

$$\dot{m}_{max} = 0.686 \frac{A^* p_t}{\sqrt{R T_t}}$$

the mass flow rate can be determined by measuring the total pressure and total temperature just upstream of the critical flow venturi (Fig. 12). The sum of the two critical flow venturi mass flow rates can then be verified by the pre-split mass flow sensor. An example is provided by the following pre-test measurements at the maximum mass flow rate for the current experiment:

- Venturi 1, p_t = 311.81 psi, T_t = 294.4 K, $\dot{m}$ = 0.284 kg/s
- Venturi 2, p_t = 305.76 psi, T_t = 299.5 K, $\dot{m}$ = 0.274 kg/s
- Mass flow sensor $\dot{m}$ =0.560 kg/s

Discrepancy between the sum of the calculated $\dot{m}$ of the venturis and the measured $\dot{m}$ of the mass flow sensor = 0.002 kg/s and the difference in $\dot{m}$ between the two supply lines is 3.6%. Agreement of the supply-line flow rates is important for spanwise lift uniformity when air is supplied to the microjets.

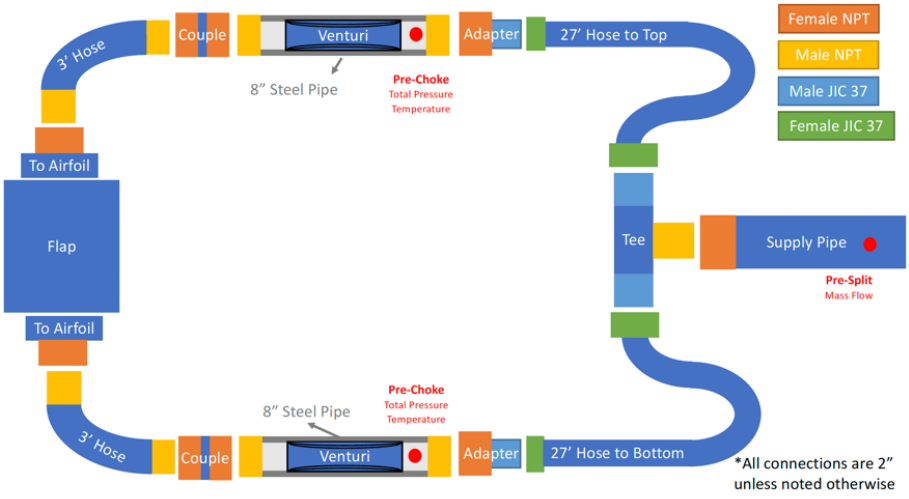

Fig. 11 Schematic of the LSWT high-pressure air supply system. System includes an upstream mass flow meter and two critical flow venturis to meter air supply to top and bottom side of the flap.

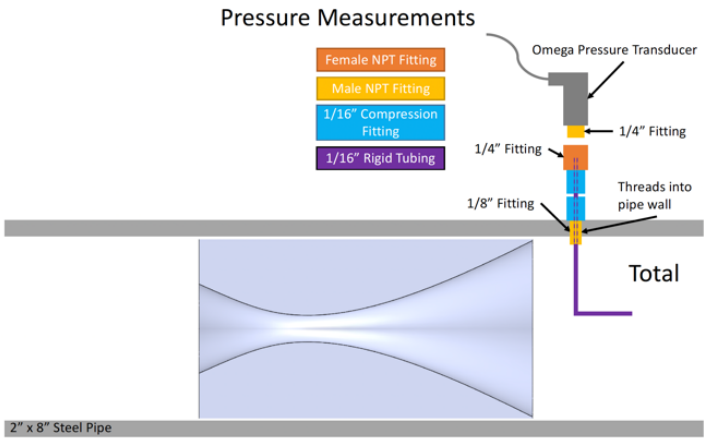

Fig. 12 Schematic of critical flow venturi.

E. Wind Tunnel Wall Effects

Lift and pitching moment results are based on integration of surface static pressure measurements. These measurements are affected by wind-tunnel walls and are typically "corrected" to remove wall effects and estimate the loads that would be measured in free flight. As described by Barlow et al.[15], a two-dimensional airfoil model that spans the wind tunnel is subject to solid and wake blockage that increase the apparent freestream dynamic pressure and wall-induced streamline curvature that increase the apparent angle of attack and camber of a lift-producing model. These corrections were applied to the data from the reference experiment on the NRL7301 with flap by Van den Berg[9] but are difficult to implement because the wake-blockage correction requires a drag measurement. In the current experiment, drag is measured using a total-pressure wake rake. However, drag measurements using this system are not correct when flow-control blowing is activated because the momentum injection due to the system is not known nor is any spanwise variability of mass or momentum injection. Furthermore, the proximity of the wake rake to the flap trailing edge in the LSWT is closer than recommended (about one-half chord). For this reason, the main results presented in Section IV are not corrected for wind-tunnel wall effects.

For cases without mass injection, wall corrections can be analyzed. Doing so for the Flap 20 configuration results in a reduction of lift coefficient of about 4.5% to 5.5% across the linear portion of the lift curve. This reduction in lift is consistent with the reduction determined using MSES[13] simulations with and without wind-tunnel walls. Applying the correction to pitching moment results in a reduction (less negative) of 6% to 8% over the same range. Again, this reduction is consistent with MSES calculations. Note, for consistency (microjet on versus microjet off), the wind tunnel results presented in Section IV are not corrected for wind-tunnel wall effects.

F. Uncertainty Analysis

The analysis of the uncertainties related to the testing of the NLR7301 with flap in the LSWT is partly based on the PhD dissertations of Ehrmann[16] and Wilcox[17]. Both authors provide detailed analyses of the uncertainty of surface-pressure-based results for two-dimensional single-element airfoil sections tested in the LSWT.

Freestream dynamic pressure was measured using a pair of static pressure rings in the wind-tunnel settling chamber and test section inlet. The difference between these rings is calibrated against a pitot-static tube in the center of the empty LSWT test section and provides the uncorrected freestream dynamic pressure to an uncertainty of ±10 Pa. Freestream static pressure was obtained using a pitot-static probe located at the test section inlet to provide freestream static pressure with an uncertainty of ±1 Pa. Model surface pressures were read with a 64-port pressure scanner with a range of ±34 kPa and an uncertainty of ±17 Pa. This scanner measured pressure differentials referenced to the static pressure of the pitot-static probe located at the inlet of the test section.

Uncertainties in tunnel dynamic pressure and airfoil surface pressures lead to uncertainties in airfoil lift and pitching moment. Representative uncertainties in the lift coefficient and pitching moment coefficient are calculated using a Monte Carlo simulation on the wind tunnel results for the NLR7301 in the Flap 20 configuration with microjet off at $\alpha = 8.0^{\circ}$, Re = 2.0 million, and $M_{\infty} = 0.10$. To perform each iteration of the simulation, pressures are randomly chosen assuming a normal distribution with mean values and standard deviations provided by the experimentally measured values and instrument uncertainties, respectively. The uncertainties in lift and pitching moment are calculated as the standard deviation of the resulting lift and pitching moment distributions, where each data point in

the distribution corresponds to a different Monte Carlo iteration. The simulation results (based on 1000 iterations) are listed in Table 1.

Table 1 Uncertainty in experimental lift and pitching moment results.

Quantity	Mean, $\overline{c_l}$	SD, σ	$\overline{c_l}/\sigma \times 100\%$	Maximum	Minimum
Lift	2.421	0.0084	0.35	2.445	2.389
Pitching moment	-0.478	0.0037	0.78	-0.465	-0.491

IV. Results

In the following sections the wind tunnel results for the model in three different configurations are presented and discussed. The first section focuses on the main element of the NLR7301 model without any flow control. In Section IV.B, results for the NLR7301 with the flap in the Flap 20 and Flap 30 configurations with microjet off are presented and discussed. For these two flap configurations, the effect of the microjet on are presented and discussed in Section IV.C. Finally, in Section IV.D several smoke flow images depicting the impact of the microjet on the flow near the flap trailing edge are presented.

A. NLR7301 Main Only (microjet off)

In this section the wind tunnel results for tests of the main element only, i.e., without the flap installed, are presented. The test was conducted at a nominal chord Reynolds number of 2.0 million and a Mach number of 0.10. The wind tunnel results are not corrected for wind-tunnel wall effects. The wall corrections are discussed in Section III.E.

Figure 13 presents the measured surface pressure distribution and the comparison with XFOIL[12] predicted pressure distribution at a c_l = 0.755. Good agreement is achieved although the XFOIL predictions are based on unbounded flow conditions whereas the present experimental results are not corrected for the presence of wind tunnel walls.

Figure 14 presents the measured lift curve and the comparison with XFOIL predicted lift curve. Good agreement is achieved but at higher angles of attack the experimental results indicate a reduction in the lift curve slope. This reduction is caused by the flow about the model becoming three-dimensional because of flow separation at the juncture of the model and the test section floor and ceiling. At high lift conditions the adverse pressure gradient on the model causes the boundary layer along the floor/ceiling to separate and this separation then extends onto the suction side of the outboard parts of the model causing the flow about the model to become three-dimensional.

Figure 15 presents the comparison between the predicted and measured pitching moment curve. The experimental results show a lower nose down pitching moment than the XFOIL predicted results which could be the result of the lack of pressure measurements in the trailing edge region of the main element as observed in Fig. 13.

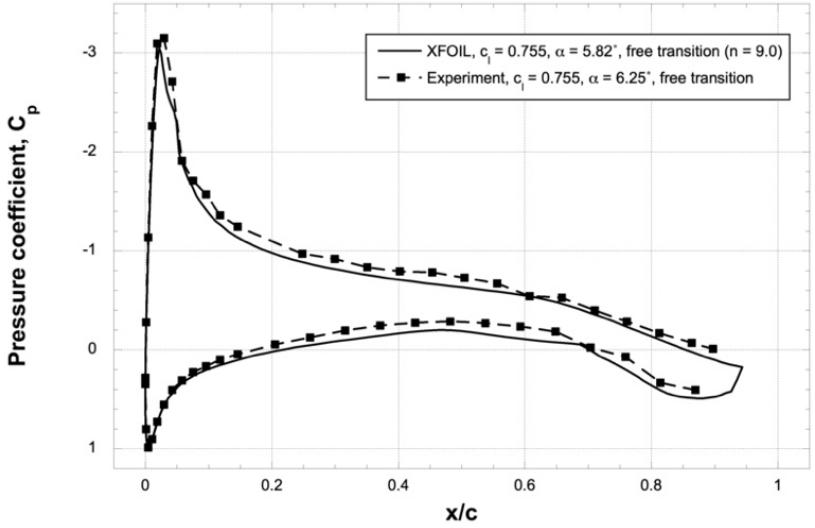

Fig. 13 Comparison of predicted and measured surface pressure distribution, main element only, c_l = 0.755, Re = 2.0 million, M_∞ = 0.10, transition free, no wind tunnel corrections applied to the wind tunnel results.

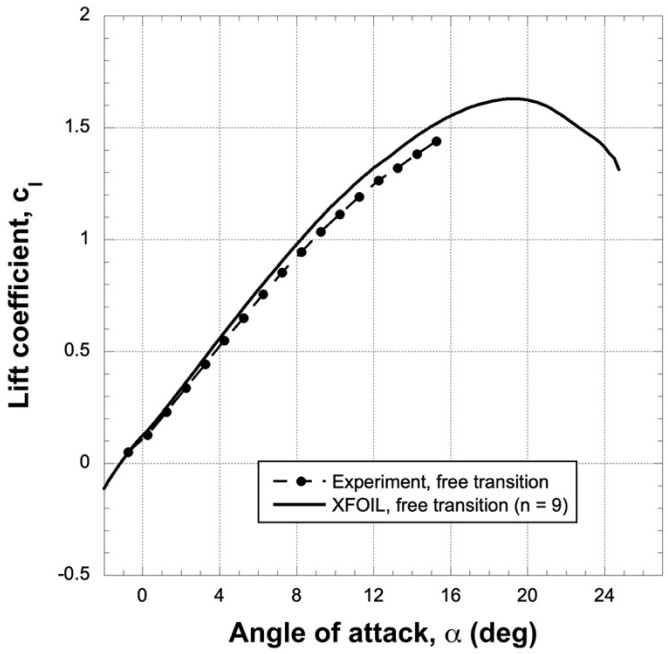

Fig. 14 Comparison of predicted and measured lift curves, main element only, Re = 2.0 million, M_∞ = 0.10, transition free, no wind tunnel corrections applied to the wind tunnel results.

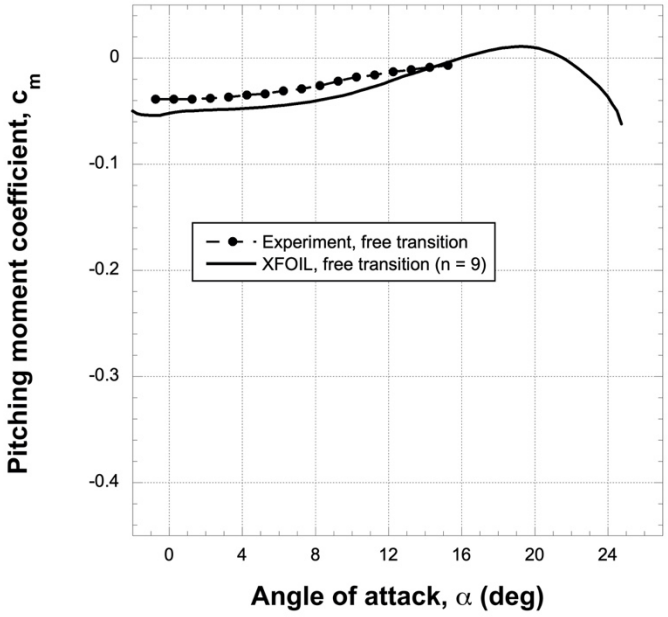

Fig. 15 Comparison of predicted and measured pitching moment curves, main element only, Re = 2.0 million, M_∞ = 0.10, transition free, no wind tunnel corrections applied to the wind tunnel results.

B. NLR7301 Main + Flap (microjet off)

In this section the wind tunnel results for the NLR7301 two-element airfoil in the Flap 20 and Flap 30 configurations are presented. The tests were conducted with the microjet off at a nominal chord Reynolds number of 2.0 million and a Mach number of 0.10. The results are not corrected for wind-tunnel wall effects. The wall corrections are discussed in Section III.E.

Figure 16 presents the measured surface pressure distribution and the comparison with experimental results for the NLR7301 two-element airfoil in the Flap 20 configuration presented by Van den Berg[9] at $c_l = 2.4$. Note, Van den Berg's pressure distribution was obtained at $\alpha = 6.0^\circ$, Re = 2.51 million, and $M_\infty = 0.185$ whereas the present experimental result was obtained at $\alpha = 8.0^\circ$ and a lower Reynolds number and Mach number. The discrepancy in angle of attack is likely the result of an apparent misalignment of the model in the test section and, at this lift condition, flow separation at the junctures of the model with the test ceiling and floor. Despite this difference in angle of attack, the mismatch in Reynolds number and Mach number, and the slight modification in the flap geometry described in Section III.C, good agreement is achieved between the two results providing confidence in the model configuration and using this model for active flow control studies.

Figure 17 presents the comparison between the Van den Berg[9] published lift curve and the current lift curve. The NLR7301 with flap is difficult to align in the wind tunnel on account of its reference chord not connecting the leading edge and trailing edge. This resulted in an apparent misalignment of approximately one degree in the linear lift regime. Except for this misalignment, good agreement is achieved until an angle of attack of approximately six degrees. At higher angles the current experimental results indicate a reduction in the lift curve slope. As already mentioned, this is caused by flow separation at the junctures of the model with the test section ceiling and floor. In the experiment conducted by Van den Berg in the NLR 3m×2m low speed wind tunnel, blowing boundary layer control was applied on the test section walls to prevent flow separation at the model tunnel wall junctures.[9]

Figure 18 presents the comparison between the Van den Berg[9] published pitching moment curve and the current pitching moment curve. The two curves show good agreement until an angle of attack of approximately six degrees.

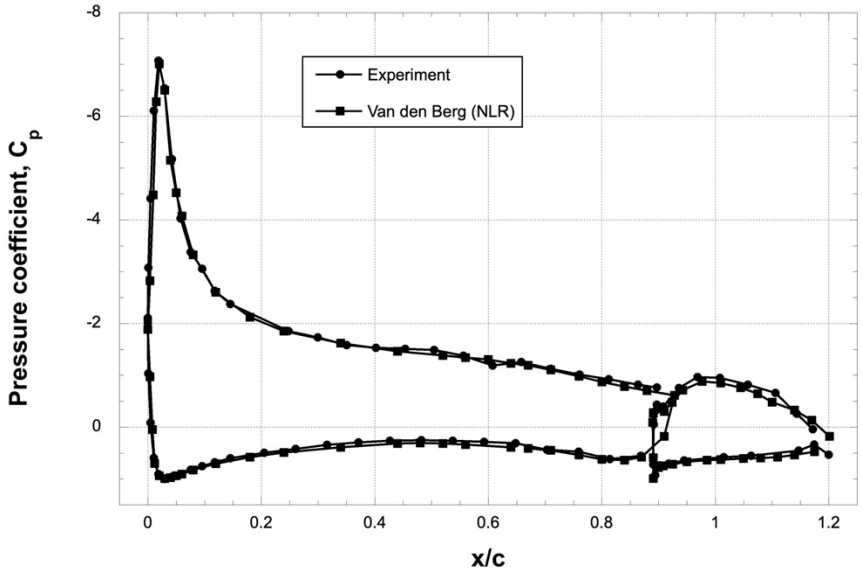

Fig. 16 Comparison of measured and NLR benchmark pressure distribution, NLR7301 two-element airfoil. Flap pressure ports shown in flap deployed location. Current Exp.: $\alpha = 8.0^\circ$, $c_l = 2.446$, Re = 2.0 million, $M_\infty = 0.10$, transition free, no wind tunnel corrections applied. NLR[9]: $\alpha = 6.0^\circ$, $c_l = 2.416$, Re = 2.51 million, $M_\infty = 0.185$, transition free, wind tunnel corrections applied.

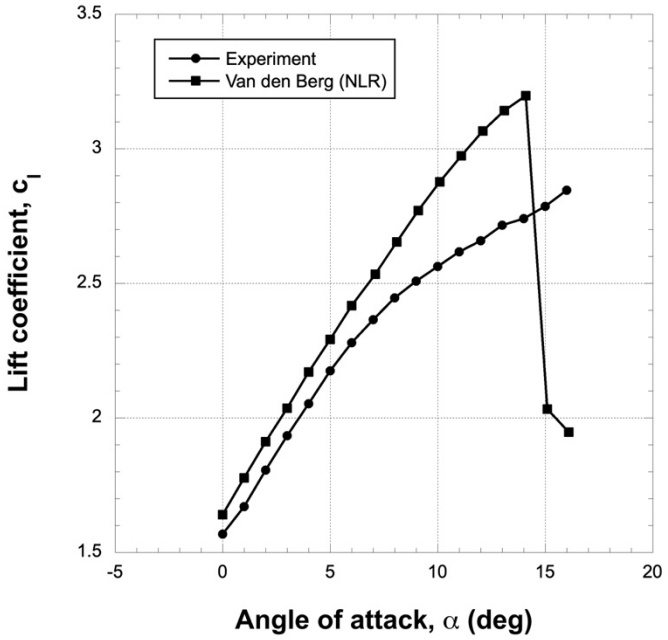

Fig. 17 Comparison of measured and NLR benchmark lift curve, NLR7301 two-element airfoil. Current Exp.: Re = 2.0 million, M_∞ = 0.10, transition free, no wind tunnel corrections applied. NLR[9]: Re = 2.51 million, M_∞ = 0.185, transition free, wind tunnel corrections applied.

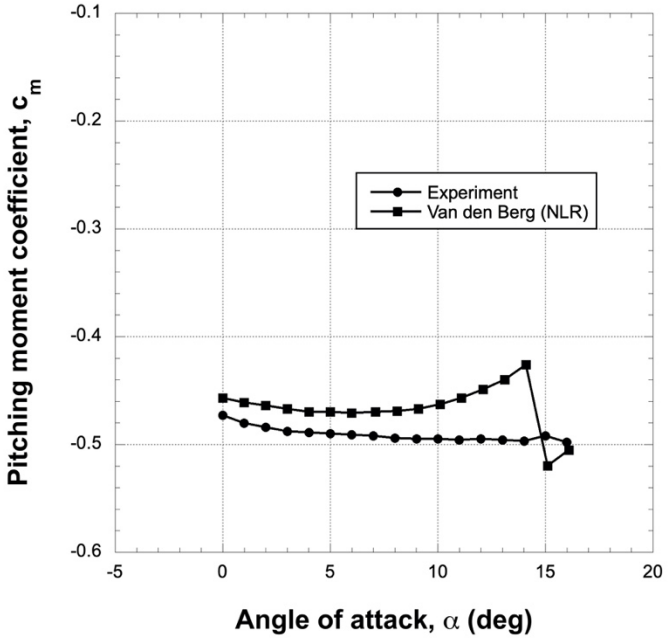

Fig. 18 Comparison of measured and NLR benchmark lift curve, NLR7301 two-element airfoil. Current Exp.: Re = 2.0 million, M_∞ = 0.10, transition free, no wind tunnel corrections applied. NLR[9]: Re = 2.51 million, M_∞ = 0.185, transition free, wind tunnel corrections applied.

Figure 19 compares the measured surface pressure distributions for the NLR7301 two-element airfoil in the Flap 20 and Flap 30 configurations at α = 8.0 deg. The flap shows the most significant change in the pressure distribution because of the 10-degree increment in its deflection.

Figure 20 compares the measured lift curves for the NLR7301 two-element airfoil in the Flap 20 and Flap 30 configurations. The increase in flap deflection angle results in a near constant increment in lift coefficient over the angle of attack range considered in this experiment.

Figure 21 compares the measured pitching-moment curves for the NLR7301 two-element airfoil in the Flap 20 and Flap 30 configurations with the higher flap loading with increasing flap deflection causing a larger nose-down pitching moment. The near parallel shift in the curves indicates little to no change in the location of the aerodynamic center of the multi-element airfoil.

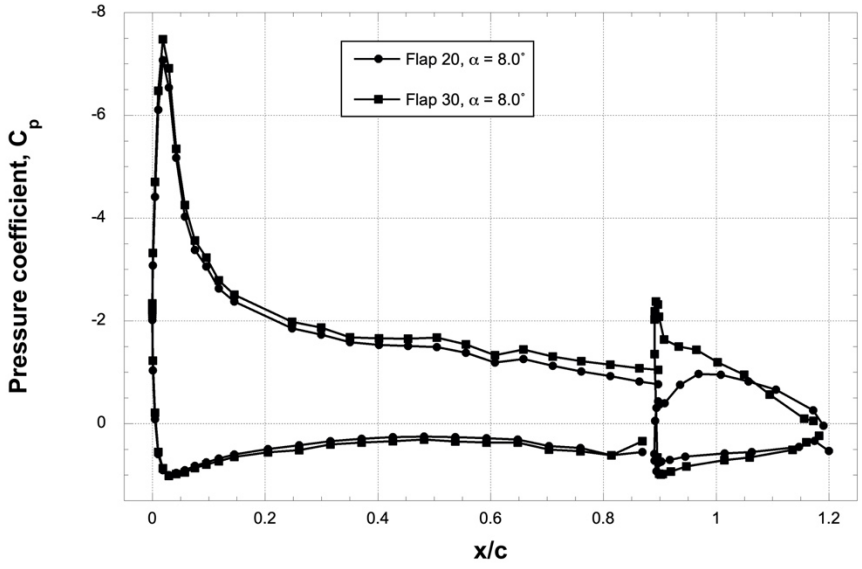

Fig. 19 Effect of flap deflection angle on pressure distributions, NLR7301 two-element airfoil, α = 8.0°, Re = 2.0 million, M∞ = 0.10, transition free, no wind tunnel corrections applied. Flap pressure ports shown in flap deployed location.

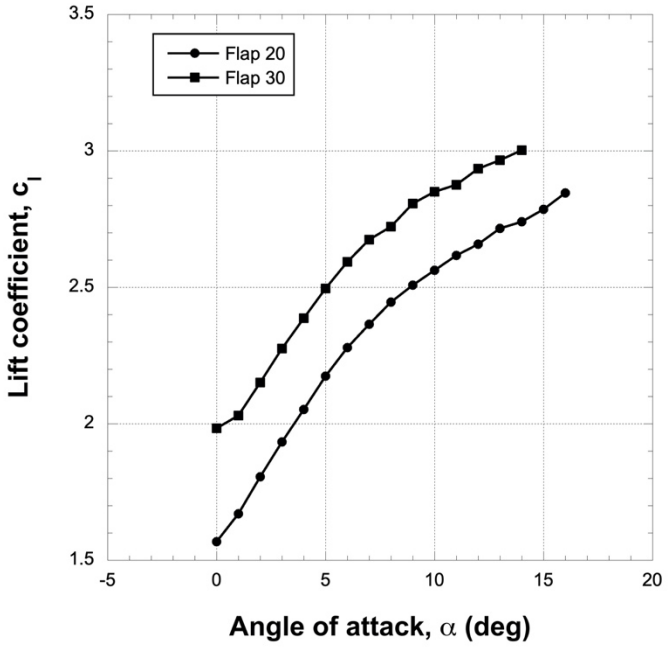

Fig. 20 Effect of flap deflection angle on lift coefficient, NLR7301 two-element airfoil, Re = 2.0 million, M∞ = 0.10, transition free, no wind tunnel corrections applied.

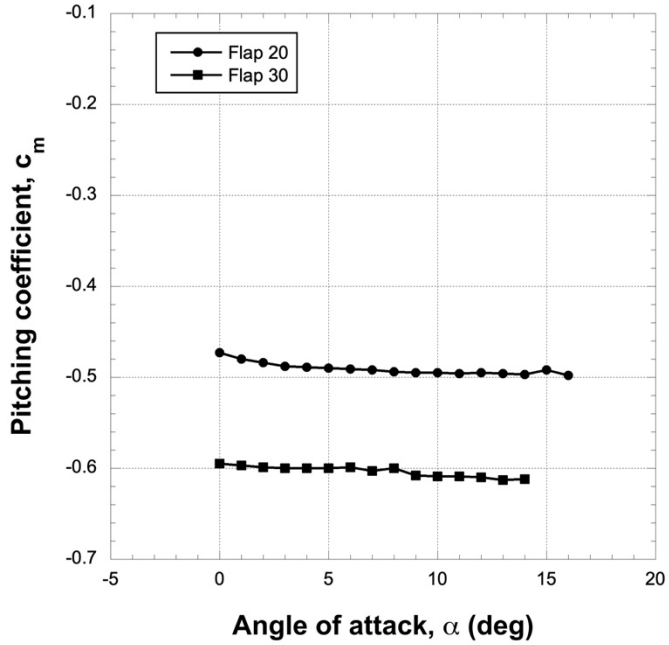

Fig. 21 Effect of flap deflection angle on pitching moment coefficient, NLR7301 two-element airfoil, Re = 2.0 million, M_∞ = 0.10, transition free, no wind tunnel corrections applied.

C. NLR7301 Main + Flap (microjet on)

In this section the wind tunnel results for the NLR7301 two-element airfoil in the Flap 20 and Flap 30 configurations with the microjet on are presented. The tests were conducted at a nominal chord Reynolds number of 2.0 million and a Mach number of 0.10. The results are not corrected for wind-tunnel wall effects. Four different microjet mass flow rates were evaluated: $C_q \approx 0.0030$, 0.0044, 0.0067, and 0.0077.

Figure 22 presents the measured surface pressure distributions and the comparison with the zero-blowing condition for the NLR7301 two-element airfoil in the Flap 20 configuration at $\alpha = 6.0^\circ$. The pressure distributions show an increase in the suction pressures for the main element and, especially, the flap with increasing mass flow rate.

Figure 23 presents the measured lift curves and the comparison with the zero-blowing condition for the NLR7301 two-element airfoil in the Flap 20 configuration. Activation of the microjet on the pressure side of the flap is effective in shifting up the lift curve of the two-element airfoil model. In the linear lift regime, the microjet effectiveness $\frac{\Delta c_l}{C_q} \simeq$ 50 for the two lower mass flow rates, however, increases to $\frac{\Delta c_l}{C_q} \simeq 65$ for the two higher mass flow rates. Note, in this experiment C_q is based on the wing reference area S thereby not accounting for the fact that the microjets only occupy 85% of the model span b.

Figure 24 presents the measured pitching moment curves and the comparison with the zero-blowing condition for the NLR7301 two-element airfoil in the Flap 20 configuration. Activation of the microjet does not change the location of the aerodynamic center. Based on the approximately zero slope of the pitching moment coefficient with angle of attack in the linear lift regime, the aerodynamic center remains very near x/c = 0.25. However, the microjet does increase the nose down pitching moment.

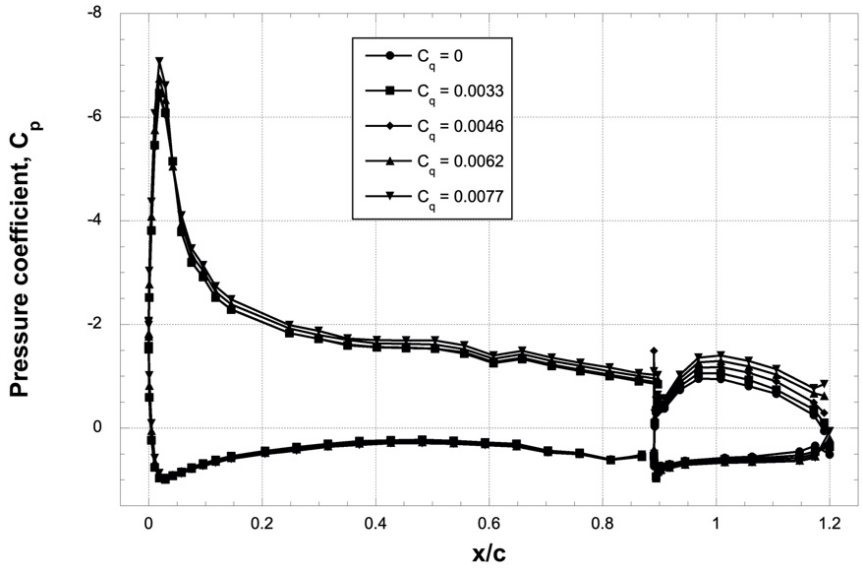

Fig. 22 Effect of microjet mass flow rate on the surface pressure distribution, NLR7301 two-element airfoil, Flap 20, α = 6.0°, Re = 2.0 million, M∞ = 0.10, transition free, no wind tunnel corrections applied. Flap pressure ports shown in flap deployed location.

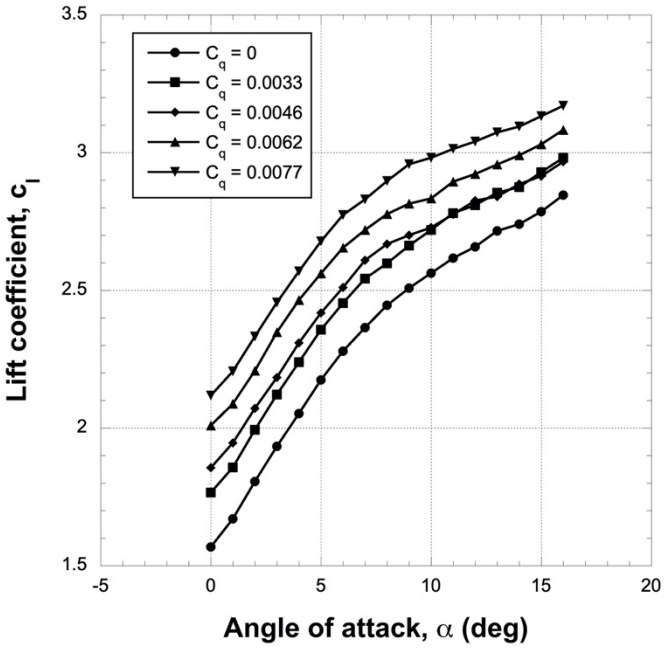

Fig. 23 Effect of microjet mass flow rate on the lift curve, NLR7301 two-element airfoil, Flap 20, Re = 2.0 million, M∞ = 0.10, transition free, no wind tunnel corrections applied.

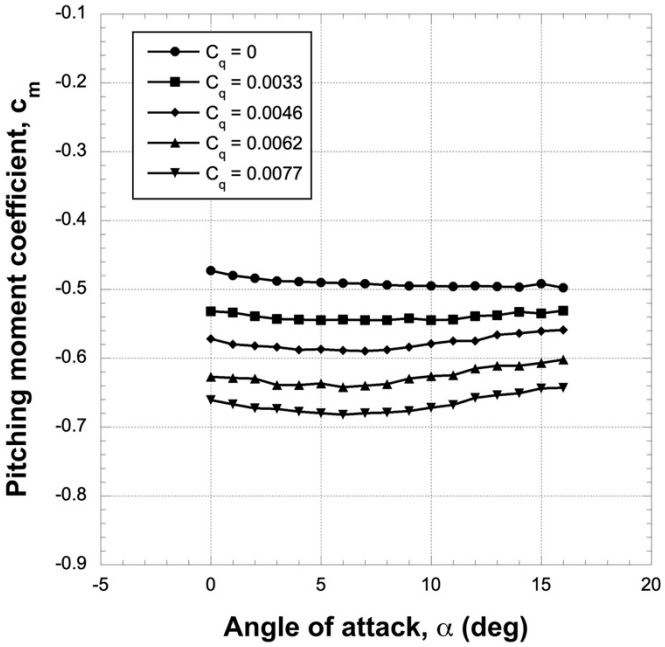

Fig. 24 Effect of microjet mass flow rate on pitching moment curve, NLR7301 two-element airfoil, Flap 20, Re = 2.0 million, M_∞ = 0.10, transition free, no wind tunnel corrections applied.

Figures 25-27 repeat the above results for the Flap 30 configuration. The measured effect of the microjets on the surface pressure distributions and the comparison with the zero-blowing condition are presented in Fig. 25. Consistent with the results for the Flap 20 configuration, the pressure distributions show an increase in the suction pressures for the main element and the flap with increasing mass flow rate.

Figure 26 presents the measured lift curves and the comparison with the zero-blowing condition. Activation of the microjet on the pressure side of the flap is effective in shifting up the lift curve of the two-element airfoil model. In the linear lift regime, at the lowest mass flow rate, the microjet effectiveness $\frac{\Delta c_l}{C_q} \simeq 38$, however, for the three higher mass flow rates the effectiveness ranges from 68-77.

Figure 27 presents the measured pitching moment curves and the comparison with the zero-blowing condition for the NLR7301 two-element airfoil in the Flap 20 configuration. Activation of the microjet does not change the location of the aerodynamic center. Based on the approximately zero slope of the pitching moment coefficient with angle of attack, the aerodynamic center remains very near x/c = 0.25 in the linear lift regime. However, the microjet does increase the nose down pitching moment.

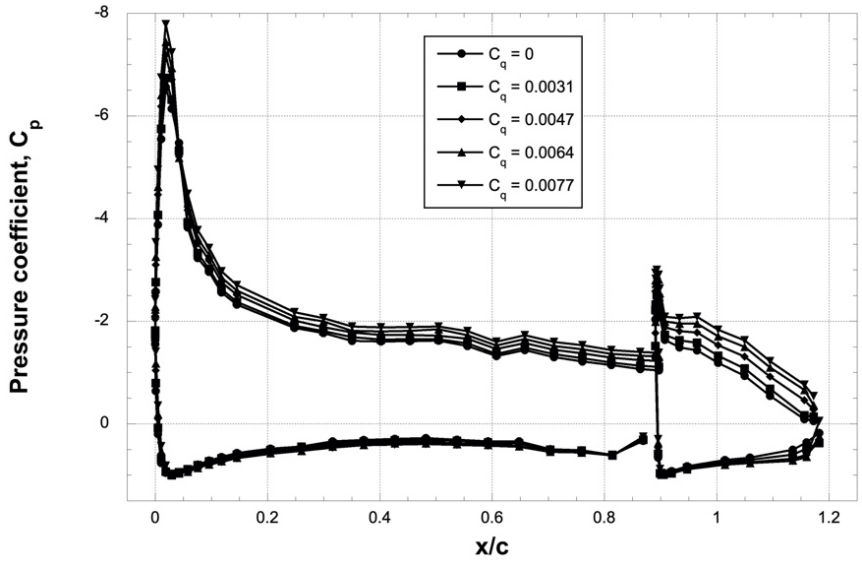

Fig. 25 Effect of microjet mass flow rate on the surface pressure distribution, NLR7301 two-element airfoil, Flap 30, α = 6.0°, Re = 2.0 million, M_∞ = 0.10, transition free, no wind tunnel corrections applied. Flap pressure ports shown in flap deployed location.

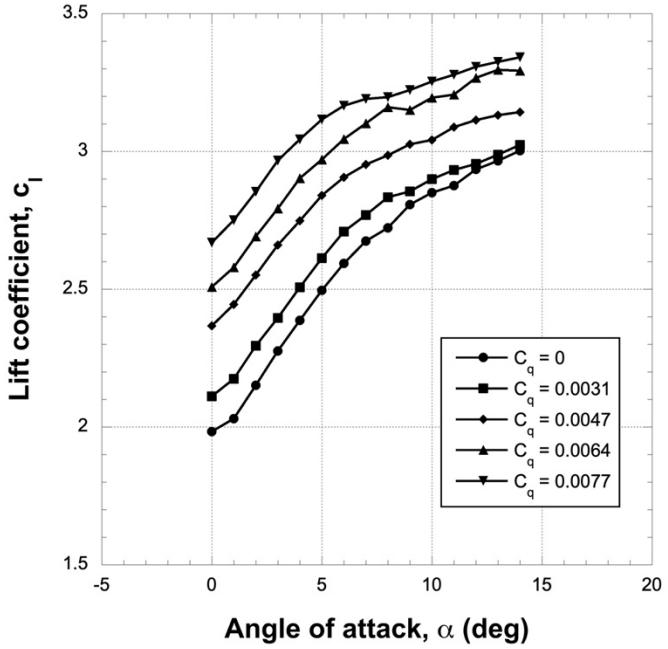

Fig. 26 Effect of microjet mass flow rate on the lift curve, NLR7301 two-element airfoil, Flap 30, Re = 2.0 million, M_∞ = 0.10, transition free, no wind tunnel corrections applied.

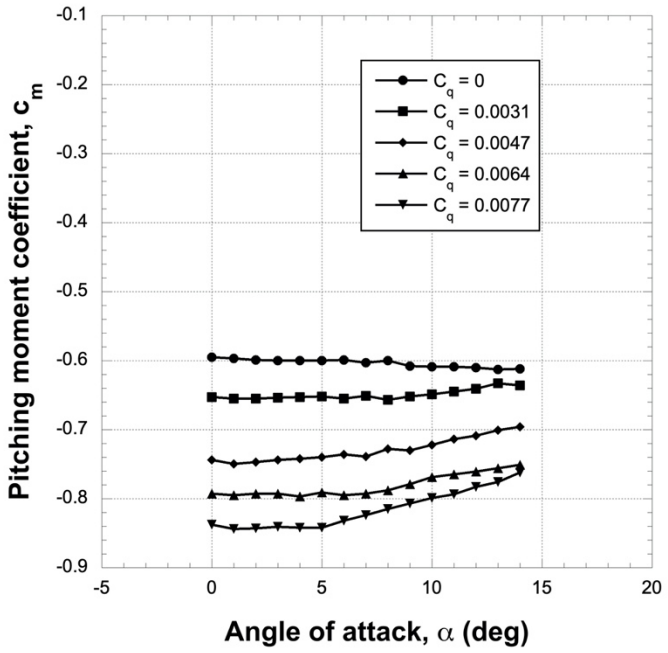

Fig. 27 Effect of microjet mass flow rate on pitching moment curve, NLR7301 two-element airfoil, Flap 30, Re = 2.0 million, M_∞ = 0.10, transition free, no wind tunnel corrections applied.

As pointed out in Hosseini et al.[2], the lift enhancement benefit of adding a microjet to the Flap 20 configuration is similar to the effect of increasing the flap deflection to Flap 30. This suggests that flap deflection and microjet blowing can be interchanged to achieve given lift performance. The results from this experiment also show this interchangeability with Fig. 28 providing an example. In Fig. 28, the pressure distribution of the Flap 30 configuration with microjet off is compared with the pressure distribution of the Flap 20 configuration with the microjet at C_q = 0.0062. Note, the lift coefficient and angle of attack are nearly identical (Flap 20, c_l = 2.65, α = 6.0˚; Flap 30, c_l = 2.62, α = 6.25˚). The surface pressures on the main element are nearly identical, however, the flap surface pressures are very different with the Flap 30 depicting a distinct leading-edge suction peak and steeper pressure recovery compared to the Flap 20. As stated earlier, this increased control of lift enables potential improvements to the overall airplane design (e.g., control of tail clearance angle) and performance (e.g., shorter field lengths, or higher payloads). It should be noted that the higher aft loading due to the microjet does cause a slight increase in the pitching moment (Flap 20, c_m = -0.624; Flap 30, c_m = -0.601).

D. Flow Visualizations

Figures 29a-d depict smoke flow visualizations for the NLR7301 two-element airfoil in the Flap 30 configuration where Fig. 29a is annotated identifying the pertinent details visible in these images. To maintain control of the smoke wand in the test section, the flow velocity had to be reduced to approximately 32% of the velocity for the results presented in Section IV.C. Given that the specified pressures (Section III.D) and, hence, mass flow rates were unchanged, this increased the microjet mass flow coefficients by a factor of approximately 3 compared to the values listed in Section IV.C. Also, the reduced airspeed decreased the Reynolds number and freestream Mach number. As a result, the smoke flow images cannot be directly linked to the results presented in Section IV.C. But they do illustrate the impact of the microjet on the flow conditions near the flap trailing edge and the increased downward flow direction (and, hence, lift) with increasing mass flow rate (increased air supply pressure ahead of the critical venturi as depicted in Fig. 12 and listed in the sub-captions of Fig. 29).

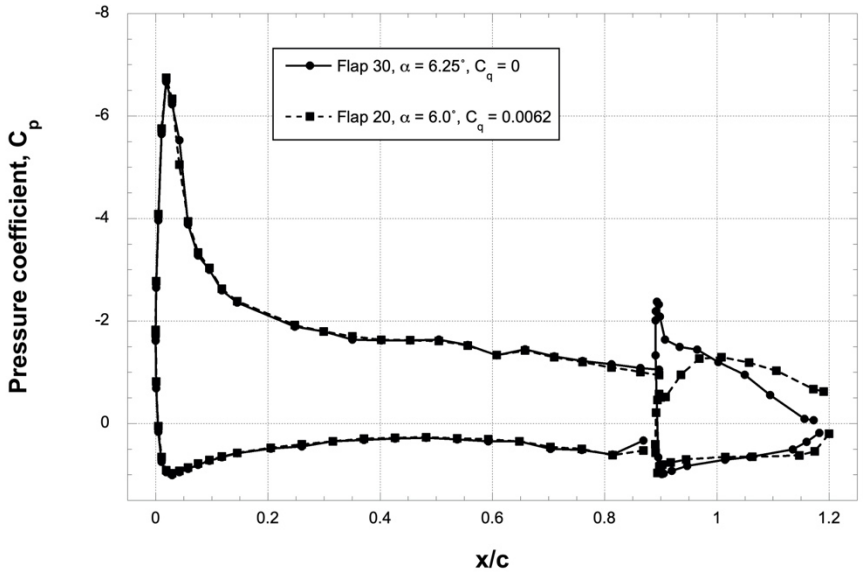

Fig. 28 Larger flap deflection with microjet off versus smaller flap defection with microjet on. NLR7301 two-element airfoil, $c_l \simeq 2.65$, Re = 2.0 million, $M_\infty = 0.10$, transition free, no wind tunnel corrections applied. Flap pressure ports shown in flap deployed location.

V. Conclusions & Next Steps

A wind tunnel model was designed, manufactured, and tested to evaluate the potential of active aerodynamic flow control for multi-element airfoils. The active flow control system involves so-called microjets – small, low momentum, normal to the surface jets located near the trailing edge of the flap – for controlling the lift and improving the aerodynamic performance characteristics of airplane high-lift systems. The configuration selected for this test is the NLR7301 two-element airfoil and it was tested in the Oran W. Nicks Low-Speed Wind Tunnel (LSWT) at Texas A&M University at a chord Reynolds number of 2.0 million and a Mach number of 0.10.

The aerodynamic performance characteristics of the baseline NLR7301 model, i.e., with the flow control system switched off, were validated by comparing the pressure distribution and sectional lift and pitching moment against published benchmark results (Flap 20 configuration) and computed results (main element only). The comparison showed good agreement providing confidence in the model configuration and using this model in the LSWT for active flow control studies.

The effect of the microjets was tested over a range of mass flow coefficients for the NLR7301 in the Flap 20 and Flap 30 configurations. The results indicate this circulation-based flow control system to be effective in terms of the change in lift coefficient over mass flow coefficient, $\frac{\Delta c_l}{C_q}$. Also, comparison of Flap 20 and Flap 30 results shows that lift enhancement because of microjet blowing at Flap 20 is similar to the effect of increasing the flap deflection to Flap 30 demonstrating that flap deflection and microjet blowing can be interchanged to achieve given lift performance. There may be spanwise variability in the slot blowing output that would not be detectable using the pressure port-based measurements. Therefore, future PIV measurements will investigate the velocity distribution in the trailing edge region of the flap including the microjet exits and the possibility of spanwise variability of the jet outputs. These measurements will also investigate the velocity distribution at the wake rake location to possibly separate the contributions of microjet momentum and model profile drag.

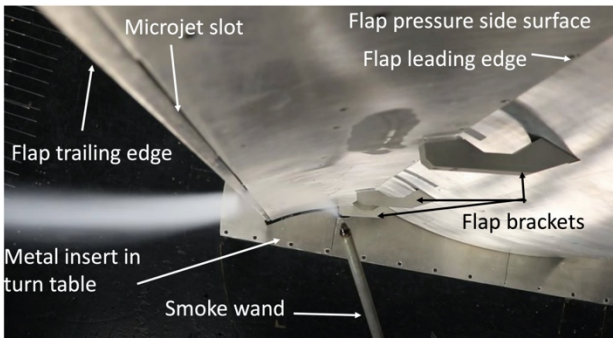

(a) Microjet off.

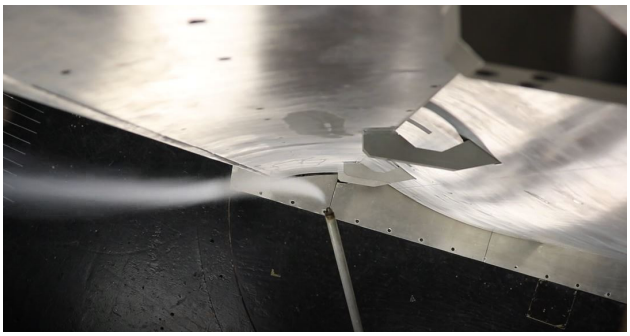

(b) Microjet air supply pressure p_t = 150 psi.

(c) Microjet air supply pressure p_t = 225 psi.

(d) Microjet air supply pressure p_t = 300 psi.

Fig. 29 Smoke flow visualization of impact of microjet mass flow on flap trailing edge flow (Flap 30, pressure side).

Acknowledgments

The research reported in this paper is funded by NASA's Advanced Air Transport Technology (AATT) project. The work by UC Davis and TAMU is funded under agreements 80NSSC19K0486 and 80NSSC20K0685 titled Microjet Normal Blowing Wind Tunnel Experiment, NASA technical monitors Shishir Pandya (ARC) and Latunia Melton (LaRC). Also, we would like to thank Aubryn Cooperman for her technical contributions and Boeing Commercial Airplanes for funding the conceptual design stage of this experiment.

References

[1] Hosseini, S.S., van Dam, C.P., and Pandya, S.A., "Aerodynamic Load Control for Multi-Element Airfoils using Surface-Normal Trailing-Edge Blowing," Journal of Aircraft, Vol. 56, No. 4, 2019, pp. 1668–1676.

[2] Hosseini, S.S., Cooperman, A.M., van Dam, C.P., and Pandya, S.A., "Microjet Configuration Sensitivities for Active Flow Control on Multi-Element High-Lift Systems," Journal of Aircraft, Vol. 58, No. 4, 2021, pp. 743–761.

[3] Malavard, L., Poisson-Quinton, P., and Jousserandot, P., "Theoretical and Experimental Investigations of Circulation Control," translated by T.M. Berthoff and D.C. Hazen, Dept. of Aeronautical Engineering, Princeton Univ. Rept. 356, Princeton, NJ, 1956.

[4] Poisson-Quinton, P., and Lepage, L., "Survey of French Research on the Control of Boundary Layer and Circulation," *Boundary Layer and Flow Control*, G.V. Lachmann (Ed.), Vol. 1, Pergamon Press, Great Britain 1961, pp. 21–73.

[5] Boeije, C.S., de Vries, H., Cleine, I., van Emden, E., Zwart, G.G.M., Stobbe, H., Hirschberg, A., and Hoeijmakers, H.W.M., "Fluidic Load Control for Wind Turbine Blades," AIAA Paper 2009-684, Orlando, FL, 2009.

[6] Blaylock, M., Chow, R., Cooperman, A., and van Dam, C.P., "Comparison of Pneumatic Jets and Tabs for Active Aerodynamic Load Control," Wind Energy, Vol. 17, No. 9, 2014, pp. 1365–1384.

[7] Meredith, P., "Viscous Phenomena Affecting High-Lift Systems and Suggestions for Future CFD Development," *High-Lift System Aerodynamics*, AGARD CP 515, September 1993, pp. 19(1)–19(8).

[8] Van Dam, C.P., "The Aerodynamic Design of Multi-Element High-Lift Systems for Transport Airplanes," Progress in Aerospace Sciences, Vol. 38, No. 2, 2002, pp. 101–144.

[9] Van den Berg, B., "Boundary Layer Measurements on a Two-Dimensional Wing with Flap," National Aerospace Laboratory, the Netherlands, NLR TR 7900911, 1979.

[10] Herring, A.K., Kutz, D.M., Brown, L.A., and White, E.B., "Upgrades to the Texas A&M Oran W. Nicks Low-Speed Wind Tunnel for M = 0.4 Operation," AIAA Paper 2015-2864, Dallas, TX, June 2015.

[11] Cooperman, A., Hosseini, S.S., and van Dam, C.P., "Task 12: Wind Tunnel Testing Options and Initial Design," report prepared for The Boeing Company, July 2019.

[12] Drela, M., "XFOIL: An Analysis and Design System for Low Reynolds Number Airfoils," *Lecture Notes in Engineering*, T.J. Mueller (Ed.), Vol. 54, 1989.

[13] Drela, M., "Newton Solution of Coupled Viscous/Inviscid Multielement Airfoil Flows," AIAA Paper 90-1479, Seattle, WA, June 1990.

[14] Burley, J.R., Bangert, L.S., and Carlson, J.R., "Static Investigation of Circular-to-Rectangular Transition Ducts for High-Aspect-Ratio Nonaxisymmetric Nozzles," NASA TP-2534, March 1986.

[15] Barlow, J. B., Rae, Jr., W. H., and Pope, A., Low-Speed Wind Tunnel Testing, 3rd ed., John Wiley & Sons, Inc., New York City, New York, 1999.

[16] Ehrmann, R.S., "Effect of Surface Roughness on Wind Turbine Performance," PhD Dissertation, Texas A&M University, August 2014.

[17] Wilcox, B.J., "Roughness Sensitivity Comparisons of Wind Turbine Blade Sections," PhD Dissertation, Texas A&M University, December 2016.